ACS central science

http://pubs.acs.org/journal/acscii

Research Article

Activity-Based NIR Bioluminescence Probe Enables Discovery of Diet-Induced Modulation of the Tumor Microenvironment via Nitric Oxide

Anuj K. Yadav,[†] Michael C. Lee,[†] Melissa Y. Lucero, Shengzhang Su, Christopher J. Reinhardt, and Jefferson Chan*

Cite This: *ACS Cent. Sci.* 2022, 8, 461−472

Read Online

ACCESS | Metrics & More | Article Recommendations | Supporting Information

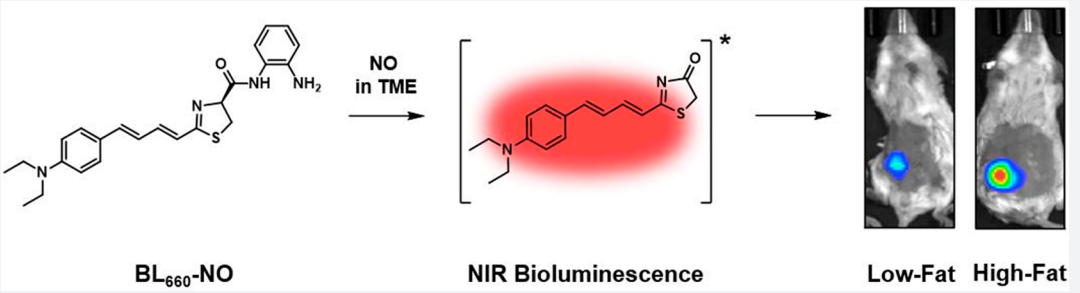

ABSTRACT: Nitric oxide (NO) plays a critical role in acute and chronic inflammation. NO's contributions to cancer are of particular interest due to its context-dependent bioactivities. For example, immune cells initially produce cytotoxic quantities of NO in response to the nascent tumor. However, it is believed that this fades over time and reaches a concentration that supports the tumor microenvironment (TME). These complex dynamics are further complicated by other factors, such as diet and oxygenation, making it challenging to establish a complete picture of NO's impact on tumor progression. Although many activity-based sensing (ABS) probes for NO have been developed, only a small fraction have been employed *in vivo*, and fewer yet are practical in cancer models where the NO concentration is <200 nM. To overcome this outstanding challenge, we have developed BL_{660}-NO, the first ABS probe for NIR bioluminescence imaging of NO in cancer. Owing to the low intrinsic background, high sensitivity, and deep tissue imaging capabilities of our design, BL_{660}-NO was successfully employed to visualize endogenous NO in cellular systems, a human liver metastasis model, and a murine breast cancer model. Importantly, its exceptional performance facilitated two dietary studies which examine the impact of fat intake on NO and the TME. BL_{660}-NO provides the first direct molecular evidence that intratumoral NO becomes elevated in mice fed a high-fat diet, which became obese with larger tumors, compared to control animals on a low-fat diet. These results indicate that an inflammatory diet can increase NO production via recruitment of macrophages and overexpression of inducible nitric oxide synthase which in turn can drive tumor progression.

INTRODUCTION

Nitric oxide (NO) is a radical species that has been implicated in vasodilation,[1] neuronal signaling,[2] immunology,[3,4] and cancer.[5] These diverse physiological and pathological roles warrant the development of tools for *in vivo* detection. This is especially true in the context of cancer, in which NO functions in various, sometimes contradictory, signaling pathways within the tumor microenvironment (TME).[6] For example, high expressions of nitric oxide synthase in activated macrophage exert cytostatic or cytotoxic effects. On the other hand, resident macrophage within the TME (i.e., tumor-associated macrophage) tend to produce low steady-state concentrations of NO (<200 nM) and are associated with a more aggressive phenotype as well as a poorer clinical prognosis.[7,8] These concentration-dependent effects suggest that other factors that modulate inflammation, such as diet, may be important in the context of cancer prevention and/or treatment.[9−13]

In vivo molecular imaging is an attractive approach to examine the contributions of inflammation in driving cancer. This extends beyond traditional means, such as measuring inducible nitric oxide synthase (iNOS) expression levels or the extent of macrophage infiltration via immunohistostaining, to provide a direct, real-time link between NO production and cancer within live animals. NO's fleeting nature remains a

Received: March 9, 2021
Published: March 16, 2022

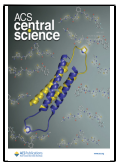

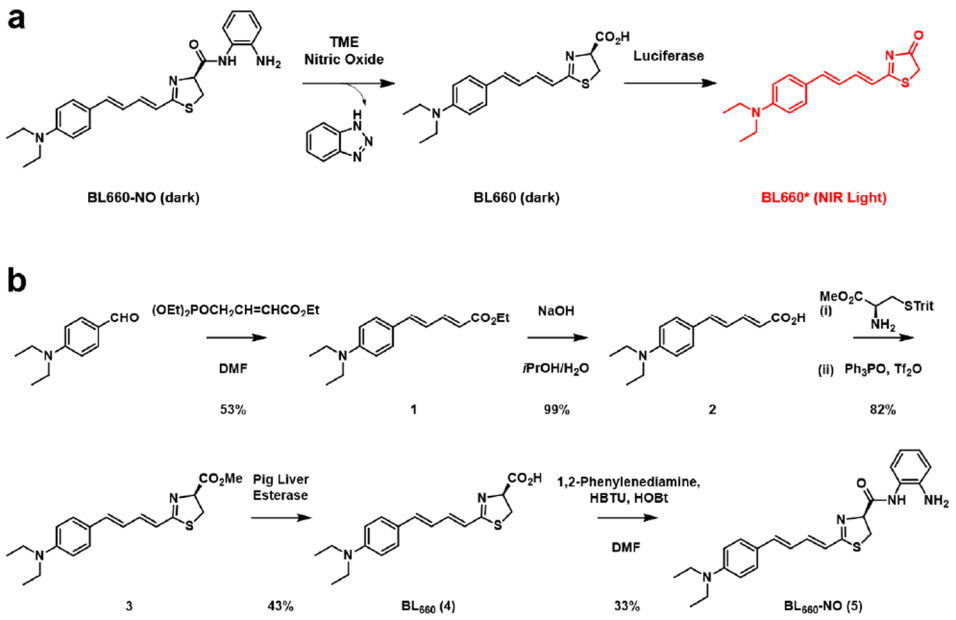

Figure 1. (a) Schematic representation of the BL_{660}-NO reaction with NO and wild-type luciferase to produce an NIR bioluminescent signal. (b) Synthesis of BL_{660}-NO.

limiting challenge in terms of live animal imaging.[6] Current techniques for directly monitoring NO *in vivo* have proven useful but have drawbacks, such as low resolution (EPR),[14,15] poor sensitivity (MRI),[16,17] or invasiveness (amperometry).[18] A complementary approach is the use of activity-based sensing (ABS) probes[19,20] which exploit the chemical reactivity of the target analyte to report on activity with high selectivity.[21−24] Until recently, most ABS probes for NO have been developed for fluorescence imaging in cellular systems.[25] In contrast, their use *in vivo* is restricted by the significant scattering of light. The transition to longer excitation and emission wavelengths (visible to NIR) reduces these effects and has facilitated several successful studies in live animals; however, most of these examples were in lipopolysaccharide (LPS) models where the concentration of NO is 10^3-fold higher than those found in cancer.[26] Our group, as well as others, has been interested in addressing these limitations in terms of both depth penetration and sensitivity. Along these lines, we developed the first ABS probe for photoacoustic imaging of NO and applied it to an LPS-induced murine inflammation model.[27] Since our work, different strategies have been reported and validated in similar models.[28,29] By rationally tuning our first-generation probe, we have designed light-activatable NO donors,[30,31] as well as new photoacoustic probes that exhibit an improved limit of detection which has allowed us to visualize endogenous NO in a murine model of breast cancer.[32,33]

Unlike fluorescence imaging (light-in, light-out) and photoacoustic imaging (light-in, sound-out), bioluminescence (BL) imaging does not rely on external light excitation to generate a readout.[34,35] As such, BL imaging offers improved sensitivity by circumventing incident light, as well as decreased background that results from autofluorescence or endogenous chromophores that are photoacoustic-active.[36] Although numerous ABS probes for BL imaging have been developed,[37,38,47,48,39−46] deep tissue imaging of NO in the TME has remained elusive. BioLeT is a notable BL probe that was employed for the detection of exogenous NO (delivered in the form of a NO donor) *in vivo*.[49] BioLeT is based on an aminoluciferin scaffold which emits visible light and therefore is best-suited for imaging at shallow depths. Recently, the development of near-infrared (NIR) BL technologies such as red-shifted substrates[50−53] and optimized luciferase enzymes[54−56] has presented exciting opportunities for deeper tissue imaging. Despite these advances, no ABS probes, for any analyte, exist for NIR BL imaging.

Herein, we report the development of BL_{660}-NO: the first ABS probe for NIR BL detection of NO in cancer. BL_{660}-NO was successfully applied for imaging in live cells and murine models of liver and breast cancer. Moreover, we employed BL_{660}-NO to investigate the effect of diet on the TME, in which a high-fat diet resulted in increased NO production as compared to a low-fat diet in mice. This work highlights the importance of studying the influence of proinflammatory stimuli in the context of cancer prevention, treatment, and progression.

RESULTS AND DISCUSSION

Design and Synthesis of BL_{660}-NO. BL_{660}-NO was designed to satisfy the following criteria to maximize *in vivo* performance. First, the emission maxima should be in the NIR range (>650 nm) to enable deep tissue imaging where scattering and attenuation of emitted light is limited. Second, the substrate should turnover rapidly in the presence of wild-type firefly luciferase (herein referred to as luciferase) to leverage established cell lines and animal models. Third, the design should be synthetically accessible, modular, and easy to diversify. With these considerations in mind, we selected AkaLumine[50] as the starting point. By exchanging the *N*,*N*-dimethyl group with other *N*,*N*-dialkyl moieties, the lipophilic character of the resulting substrates can be tuned to maximize tumor accumulation.[57] For instance, in comparison to AkaLumine, the *N*,*N*-diethyl analogue (BL_{660}) produced significantly higher BL signals when A549-Luc2 and 4T1-Luc cells were incubated with equimolar concentrations of both substrates (Figures S1 and S2). Moreover, we found that BL_{660}

https://doi.org/10.1021/acscentsci.1c00317
ACS Cent. Sci. 2022, 8, 461−472

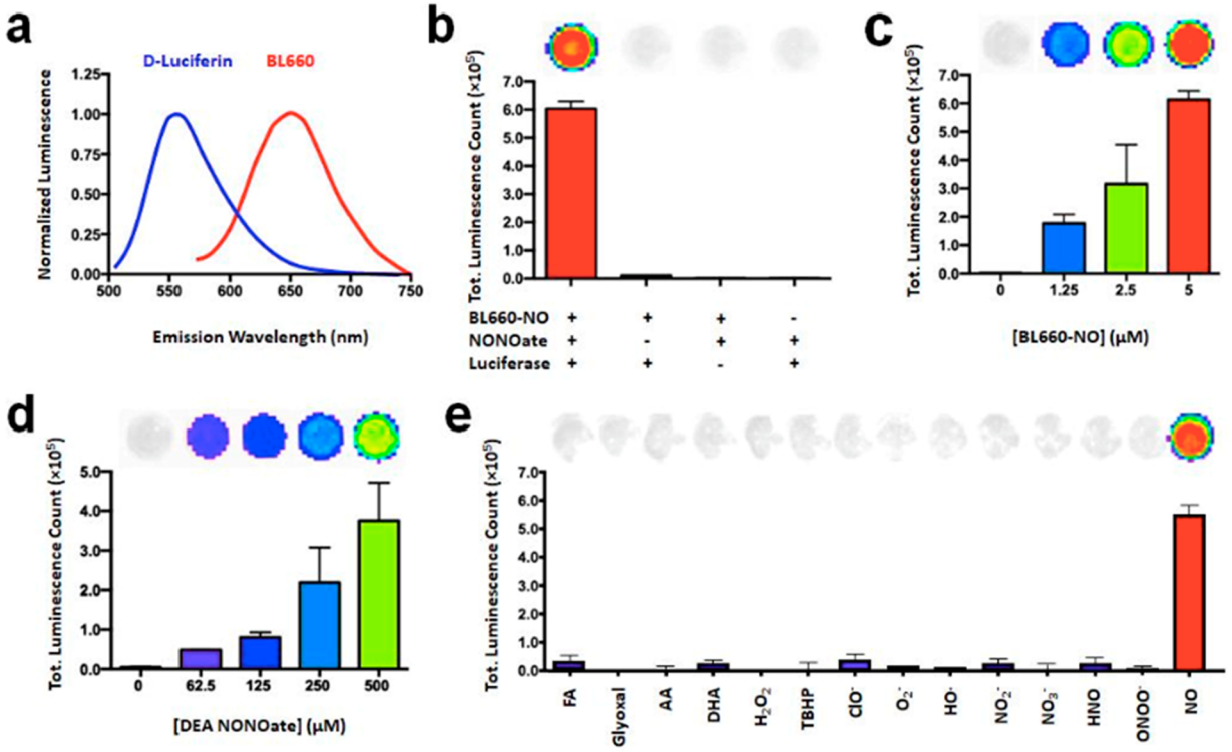

Figure 2. (a) Spectra of luciferin and BL_{660} in the presence of recombinant luciferase. (b) *In vitro* assay demonstrating that the probe, NO, and luciferase must all be present to generate a signal: BL_{660}-NO (5 μM), DEA NONOate (250 μM), and luciferase (0.05 mg/mL). (c) Bioluminescent signal as a function of BL_{660}-NO concentration (0, 1.25, 2.5, 5 μM). (d) Bioluminescent signal as a function of DEA NONOate concentration (0, 62.5, 125, 250, 500 μM). (e) Selectivity assay against a panel of biologically relevant analytes. All analytes were present in 75-fold excess relative to BL_{660}-NO (5 μM). All data is reported as the mean ± standard deviation (n = 3).

was stable in cell culture media for up to 12 h (Figure S3). We hypothesized that capping the carboxylate group with a NO-responsive unit (e.g., *o*-phenylenediamine trigger)[58] would prevent enzymatic activity with luciferase. However, the reaction with NO (via the active species N_2O_3) is expected to be rapid en route to generate an acyl triazole intermediate, which can undergo spontaneous rate-limiting hydrolysis to yield BL_{660}. The resulting substrate can then react with luciferase (K_m = 5.54 ± 0.95 μM) to generate BL in the NIR range (λ_{em} = 660 nm) (Figure 1a and Figure S4). This is critical because it means that our probe is compatible with any luciferase expressing cell line. An added benefit of this design strategy is that it masks the negative charge and should facilitate rapid uptake, as opposed to substrates such as luciferin.

The synthesis[50,59] of BL_{660}-NO began with the Horner–Wadsworth–Emmons olefination reaction between 4-diethylaminobenzaldehyde and triethyl 4-phosphonocrotonate to afford the conjugated *trans*-diene ester **1** in 53% yield. Hydrolysis of the ester to the corresponding carboxylic acid proceeded quantitatively in acetonitrile–water to yield acid **2**. Condensation of **2** with *S*-trityl protected D-cysteine methyl ester, followed by cyclization in the presence of trifluoromethanesulfonic anhydride and triphenylphosphine oxide, furnished the thiazoline methyl ester intermediate **3** in 82% yield. Hydrolysis of the methyl ester group with pig liver esterase afforded the free acid **4** (BL_{660}) in 43% yield. Finally, **4** was coupled to *o*-phenylenediamine using *O*-(benzotriazole-1-yl)-*N*,*N*,*N*′,*N*′-tetramethyluronium hexafluorophosphate (HBTU) to afford the final probe, BL_{660}-NO, in 33% yield (Figure 1b).

We also prepared a nonresponsive control compound (Ctrl-BL_{660}-NO) to confirm the proposed NO- and luciferase-dependent activation. Ctrl-BL_{660}-NO was synthesized using the same reaction sequence above; however, we employed *m*-phenylenediamine, instead of the *o*-phenylenediamine trigger, because it cannot form the labile acyl triazole intermediate necessary to generate BL_{660} (Figure S5).

***In Vitro* Characterization.** With BL_{660} and BL_{660}-NO in hand, we first obtained a bioluminescent spectrum of BL_{660} which revealed that the emission maximum is separated from the corresponding maximum of luciferin (λ_{em} = 560 nm) by 100 nm (Figure 2a). Next, we examined the response of BL_{660}-NO to NO and recombinant luciferase *in vitro* by incubating the probe with a NO donor (DEA NONOate, 250 μM) for 30 min (pH 8 and 37 °C). The reaction mixture was then treated with ATP-$MgSO_4$ and luciferase (0.05 mg/mL). We confirmed via LCMS analysis that BL_{660} and the benzotriazole byproduct were being generated, consistent with the proposed activation mechanism (Figure S6). We further demonstrated that both NO and luciferase were essential to generate a BL signal (Figure 2b). Linear relationships were observed between the BL signal and either probe or NO concentration while holding the other parameter constant (Figure 2c,d).

Next, we tested the selectivity of BL_{660}-NO by incubating it with various biologically relevant analytes in the presence of luciferase. For instance, we evaluated its reactivity with several reactive carbonyl species (i.e., formaldehyde, glyoxal, acetaldehyde, dehydroascorbic acid) which can generate various cyclized products.[60−62] Moreover, we tested a panel of reactive oxygen species (i.e., hydrogen peroxide, *tert*-butyl hydrogen

https://doi.org/10.1021/acscentsci.1c00317
ACS Cent. Sci. 2022, 8, 461−472

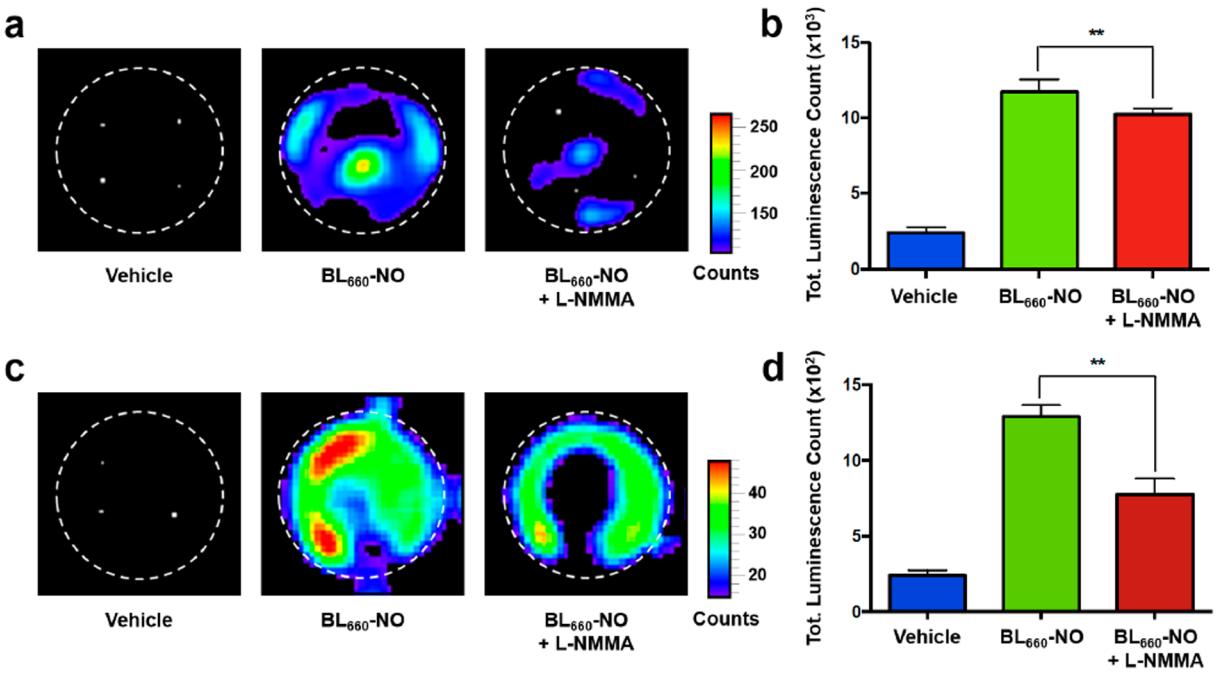

Figure 3. (a) Representative images of BL signals from A549-Luc2 cells upon treatment with vehicle (DMSO), BL_{660}-NO (10 μM), or pretreatment with inhibitor L-NMMA (1 mM) for 30 min followed by BL_{660}-NO (10 μM). (b) Quantified data from panel a. (c) Representative images of BL signals from 4T1-Luc upon treatment with vehicle (DMSO), BL_{660}-NO (10 μM), or pretreatment with inhibitor L-NMMA (1 mM) for 30 min followed by BL_{660}-NO (10 μM). (d) Quantified data from panel c. All data is reported as the mean ± standard deviation (n = 3). Color scales represent luminescence counts. The exposure time, 60 s; emission, open; binning factor, 8; and f number, 1. Dotted white circles represent ROIs used for quantification. A statistical analysis was performed using Student's t-test (α = 0.05), **: $p < 0.01$.

peroxide, hypochlorite, superoxide anion, hydroxyl radical) and reactive nitrogen species (i.e., nitrite, nitrate, nitroxyl, peroxynitrite) that could react with the substrate component or the trigger to give undesirable activation. Negligible changes (<6%) in the bioluminescent signal were observed with up to 75-fold molar excess of each species, consistent with exceptional selectivity (Figure 2e). In contrast, treatment of BL_{660}-NO with NO resulted in a robust signal enhancement. Lastly, prior to incubation with luciferase, we treated BL_{660}-NO with fatty acid amide hydrolase (FAAH) and cyclooxygenase-2 (Cox-2) since both of these enzymes can potentially hydrolyze the amide bond of BL_{660}-NO. Relative to activation by DEA NONOate (50-fold), there was only an 18.6% signal enhancement with FAAH and no change with Cox-2 (Figure S7).

Detection of NO in Cancer Cells with BL_{660}-NO. Next, we evaluated the responsiveness of BL_{660}-NO toward endogenous NO in human A549-Luc2 lung cancer cells and murine 4T1-Luc breast cancer cells. Of note, the detection of basal levels of NO in cell culture is challenging owing to the absence of an external stimulus (e.g., TME) that can induce the overexpression of iNOS and subsequent overproduction of NO. Cells were treated with 10 μM BL_{660}-NO and imaged immediately. Within a few minutes, the cells became bioluminescent compared to vehicle controls (Figure 3a–d). To determine if this turn-on response was due to NO, we pretreated cells with L-NMMA, a reversible competitive inhibitor of human and murine NOS, before application of BL_{660}-NO.[63] We observed a statistically significant decrease in the bioluminescent signal for both cell lines under these conditions (Figure 3a–d). Moreover, we found that L-NMMA did not exhibit any inhibitory effect on the BL of BL_{660} (Figure S8). Together, these results are important because they indicate that BL_{660}-NO exhibits the exceptional sensitivity necessary to detect NO at basal levels, even within cell cultures. Before applying BL_{660}-NO *in vivo*, we performed standard MTT assays to assess its potential cytotoxicity. Cells were incubated with BL_{660}-NO at various concentrations (0–20 μM) for up to 3 h. Even at the highest concentration of probe, we did not observe significant loss of cell viability (Figure S9), indicating that BL_{660}-NO would be suitable for *in vivo* applications.

Evaluation of BL_{660}-NO in Liver and Breast Cancer Models. First, we inoculated Nu/J mice with A549-Luc2 cells using an intrahepatic procedure to generate heterotopic lung tumors.[76] This experiment served to answer whether BL_{660}-NO exhibits sufficient sensitivity to extend into deep tissue (i.e., beyond the subcutaneous space). After 11 weeks, mice were treated with BL_{660}-NO and imaged using the IVIS imaging system. The BL signals from the liver were clearly evident while there was no signal from nontumor control animals (Figure S10). To confirm that BL_{660}-NO can detect endogenous NO in A549-Luc2 tumors, we inoculated a second set of mice via subcutaneous injection. After 4 weeks, tumors were intratumorally treated with either saline (control) or L-NMMA 1 h prior to imaging with BL_{660}-NO (Figure 4a). Although not statistically significant, the resulting trend demonstrates a reduction in the BL signal for the animals receiving the iNOS inhibitor and thus suggests that BL_{660}-NO is being activated by NO (Figure 4b). While these two studies allowed us to evaluate our probe in a human cancer cell line, it is important to note that nude mice lack a functional immune system which is critical for establishing the TME. For this reason, subsequent experiments were performed in syngeneic murine models.

https://doi.org/10.1021/acscentsci.1c00317
ACS Cent. Sci. 2022, 8, 461–472

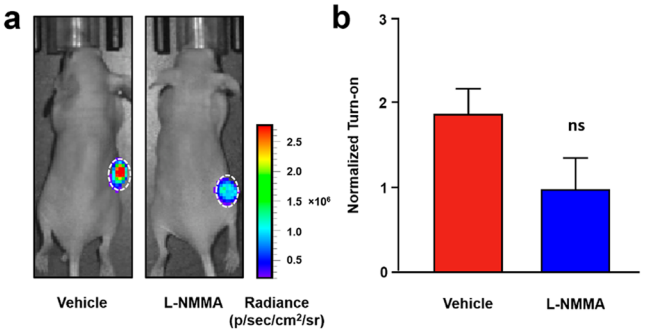

Figure 4. (a) Representative BL images of mice pretreated with a vehicle control (saline) or L-NMMA (35 mM, 50 μL). (b) Normalized data from panel a. Vehicle treatment data is reported as the mean ± standard deviation (n = 3), and L-NMMA treatment data is reported as the mean ± standard deviation (n = 5). Exposure time, 25 s; emission, 660 nm; binning factor, 8; and f number, 1. Dotted white ovals represent ROIs used for quantification. A statistical analysis was performed using Student's t-test (α = 0.05). No statistical significance was observed.

In particular, we established a heterotopic 4T1-Luc breast cancer allograft model in BALB/c mice via subcutaneous injection in the flank. The tumors were allowed to grow to 300−400 mm^3 (∼30 days). BL_{660}-NO was then administered systemically, and the BL signal was monitored (Figure 5a). We

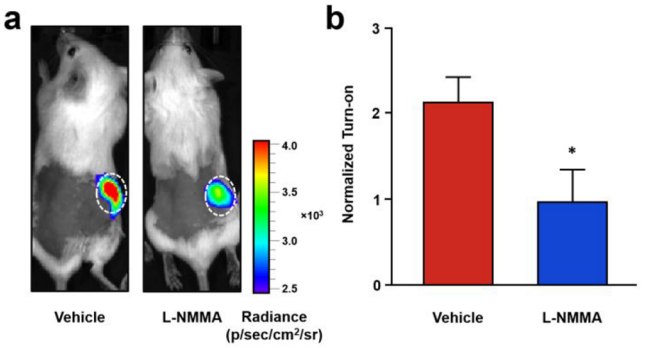

Figure 5. (a) Representative BL images of mice pretreated with a vehicle control (saline) or L-NMMA (35 mM, 50 μL). (b) Normalized data from panel a. All data is reported as the mean ± standard deviation (n = 3). Exposure time, 60 s; emission, open; binning factor, 8; and f number, 1. Dotted white ovals represent ROIs used for quantification. A statistical analysis was performed using Student's t-test (α = 0.05), *: $p < 0.05$.

observed a signal enhancement in the tumor region that persisted for at least 2 h. As before, to verify that this was due to NO, we divided the tumor-bearing mice into two groups which were treated with a vehicle control (saline) or L-NMMA prior to administration of BL_{660}-NO. We hypothesized that the NOS inhibitor would attenuate the BL signal if NOS-derived NO was responsible for the probe activation. We observed a turn-on response of 2.2 ± 0.3 (defined as the ratio of the BL signal at 1 h relative to immediately after BL_{660}-NO treatment) in the vehicle group. In comparison, we did not note any change in the signal intensity of the L-NMMA treatment group (Figure 5b). To further corroborate our results, we introduced Ctrl-BL_{660}-NO, a nonresponsive isomer of our probe, and BL_{660}-NO via intratumoral injection. We selected this route of administration as opposed to systemic injection to account for possible differences in biodistribution and uptake into the tumors. As anticipated, we did not observe any signal enhancement relative to BL_{660}-NO (Figure S11).

Effect of Diet on NO Generation in a Heterotopic Breast Cancer Model with BL_{660}-NO. Numerous studies have suggested that high-fat diets are a risk factor for breast cancer because they promote chronic inflammatory states.[12,64−69] For instance, a recent study of 337 000 women found that those who ate the most saturated fat were approximately 30% more likely to develop breast cancer compared to their counterparts who ate the lowest levels.[70] However, relating these findings to a molecular entity, such as NO, has not been possible to date. With the development of BL_{660}-NO, we sought to design an experiment to determine the impact of a high-fat diet on inflammation, NO generation in the TME, and tumorigenesis. Specifically, we elected to employ an orthotopic breast cancer model since this would allow us to study the effects of diet in the native TME. First, we randomly divided female BALB/c mice into two groups to be fed low-fat and high-fat diets, in which 10% and 60% of calories are from fat, respectively, for 12 weeks. Of note, we did not control their caloric intake by allowing the mice to feed freely to mimic the variable food consumption behavior of humans. After this period, 4T1-Luc cells were injected into the mammary fat pads, and the same diets were continued until the end of the study (Figure 6a). Consistent with previous reports, the mice in the high-fat group became obese and were 60% heavier (39.7 ± 3.9 g vs 23.1 ± 0.8 g). Moreover, the tumor volumes of the low-fat and high-fat diet groups were measured to be 176.7 ± 41.5 and 223.9 ± 74.3 mm^3, respectively. This raises an important consideration; that is, since the tendency for high-fat animals is to have larger tumors on average, would the presence of more luciferase expressing cancer cells give confounding results since it would be difficult to determine if a higher BL signal is due to more NO or more luciferase.

To distinguish this, we designed a cell-based study where we performed BL imaging with BL_{660}-NO and luciferin. We hypothesized that the ratio between luciferin emission and BL_{660}-NO emission (560/660) would be constant at a given NO concentration, and it should not depend on the number of cells present if the sensing of NO is rate-limiting. In contrast, if the number of cancer cells effects the 560/660 ratio, this would indicate that BL_{660}-NO was reporting on luciferase levels instead of NO and, thus, may be ineffective when tumor sizes differ. We tested this by treating one, two, or three million 4T1-Luc cells/mL with either 62.5, 125, or 250 μM DEA NONOate. The cells were then incubated with BL_{660}-NO and imaged using the 660 nm filter set on the IVIS imaging system. Likewise, a second set of cells were treated with luciferin and imaged using the 560 nm filter set. We found that the 560/660 ratio did not change as a function of cell number (Figure S12a). However, as the DEA NONOate concentration increased from 62.5 to 125 to 250 μM, the mean 560/660 ratio (obtained by averaging the ratio at different cell numbers) decreased in a concentration-dependent manner (Figure S12b). To confirm that DEA NONOate was not exerting an unanticipated effect on luciferase activity, we preincubated 4T1-Luc cells with either a vehicle or the NO donor prior to treatment with luciferin or BL660. In both instances, the BL signal intensity was not impacted by the presence of DEA NONOate (Figure S13). Moreover, we implanted 4T1-Luc cells in a new group of animals and performed imaging at three

https://doi.org/10.1021/acscentsci.1c00317
ACS Cent. Sci. 2022, 8, 461−472

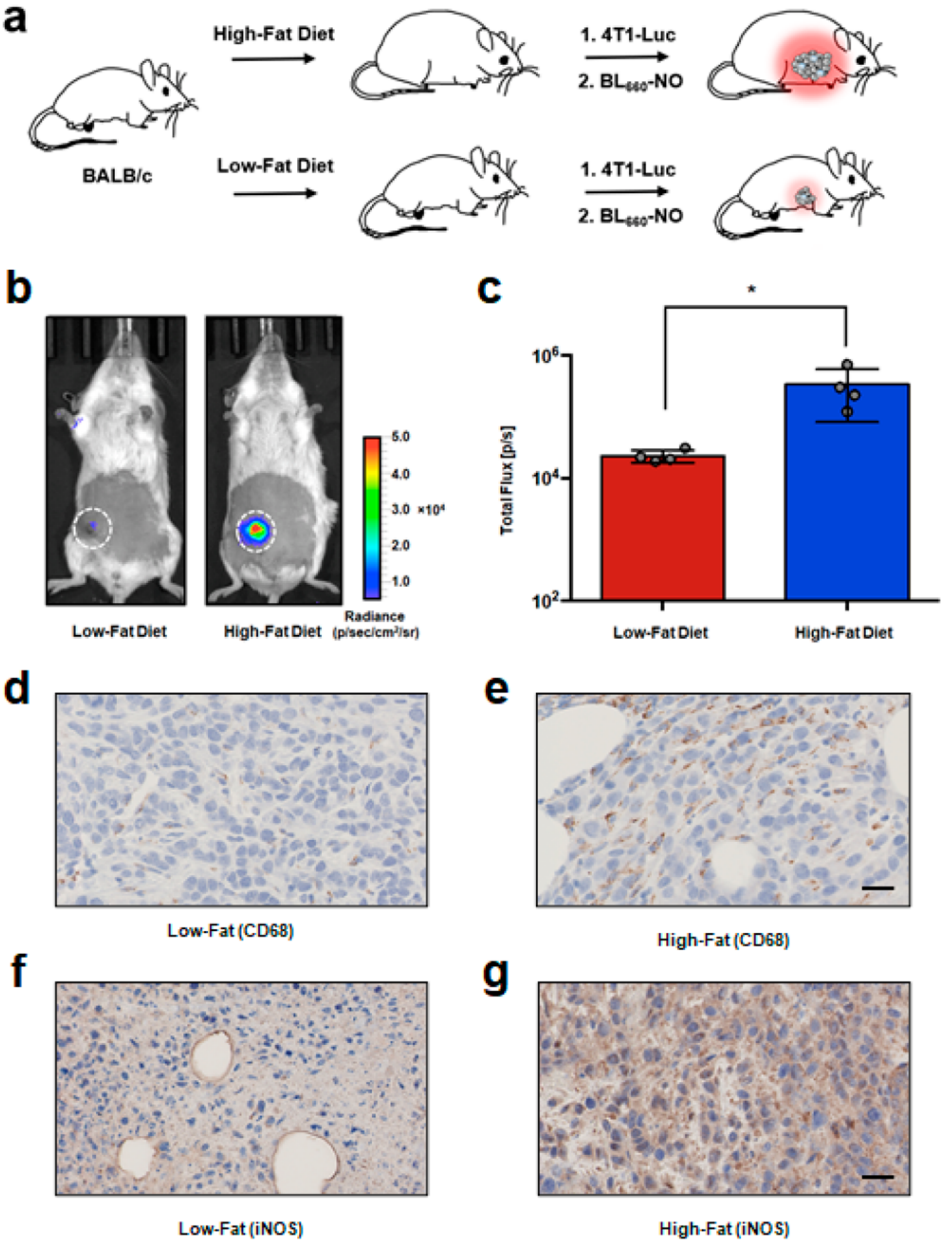

Figure 6. (a) Schematic representing the workflow for the generation of mouse models to study the effect of diet on tumorigenesis and NO production by BL imaging. (b) Representative BL images of mice on low-fat and high-fat diets for 24 weeks, respectively, upon treatment with BL_{660}-NO. (c) Quantified data from panel b. All data is reported as the mean ± standard deviation (n = 4). Exposure time, 60 s; emission, open; binning factor, 8; and f number, 1. Dotted white ovals represent ROIs used for quantification. A statistical analysis was performed using Student's t-test (α = 0.05), *: $p < 0.05$. Representative images of tumors excised from mice fed a (d) low-fat diet and (e) high-fat diet for 24 weeks with CD68 staining. Scale bar = 25 μm. Representative images of tumors excised from mice fed a (f) low-fat diet and (g) high-fat diet for 24 weeks with iNOS staining. Scale bar = 25 μm.

tumor volumes (104.9 ± 20.0, 156.7 ± 24.4, and 253.5 ± 19.0 mm^3). We hypothesized that we would not observe a tumor volume-dependent increase in the BL signal if differential activation of BL_{660}-NO was due to changes in NO levels. Indeed, we did not record statistically significant differences as a function of tumor volume (Figure S14). Together, these results are consistent with NO detection being rate-limiting, which is an important feature of our probe design. Moreover, we designed a control experiment to investigate whether factors independent of NO (e.g., uptake and accumulation of the probe in fatty tissue) could yield a difference in BL. Specifically, BL_{660} (the turned over product) was employed to image tumors in the high-fat and low-fat diet groups. As shown in Figure S15, the two groups were indistinguishable.

With these results, we proceeded to image NO with BL_{660}-NO, 60 min after probe administration. We found that the BL signal was on average 2.63-fold higher in mice fed the high-fat diet (9883.7 ± 4014.4) than in those fed the low-fat diet (3756.4 ± 3063.4) (Figure S16). Animals were sacrificed after imaging to harvest their tumors for further analysis. Tumors were subjected to immunohistochemical analyses of CD68, a protein overexpressed in circulating macrophages and tissue macrophages. We observed positive CD68 staining in the tumors of the high-fat mice that was higher than that in the

https://doi.org/10.1021/acscentsci.1c00317
ACS Cent. Sci. 2022, 8, 461−472

low-fat tumors (Figures S17 and S18). These results indicate that a high-fat diet is correlated with increased macrophage infiltration. Likewise, we noted significantly greater iNOS staining in the tumors of mice from the high-fat diet condition (Figures S19 and S20). Together, these results suggest that the consumption of a high-fat diet over a 12 week period promotes an inflammatory response within the TME that is linked to an increase in the number of tumor-associated macrophage and the overexpression of iNOS, which in turn are responsible for the elevated levels of NO that was detected by BL_{660}-NO. Despite these promising results, we designed and conducted a second study where the diet-priming period was increased from 12 to 24 weeks since numerous reports have demonstrated that this would result in a more profound inflammatory response.[71,72] Additionally, the time frame between probe administration and image acquisition was decreased from 60 min (initial study) to 30 min. We identified this optimized incubation time using Ctrl-BL_{660}-NO, which was administered systemically to mice fed high-fat and low-fat diets. Specifically, at 30 min, there was no activation or a statistically significant difference between the two groups (Figures S23 and S24). Results from this second study revealed a greater BL signal increase in the mice fed a high-fat diet (14.8 ± 4.7-fold; 3.4 ± 2.5 × 10^5 cf. 2.3 ± 0.5 × 10^4) compared to the 12 week study owing to higher levels of NO. Likewise, when we performed immunohistostaining for CD68 (26.2 ± 3.0% cf. 8.9 ± 3.4%) and iNOS (46.2 ± 10.1% cf. 16.1 ± 5.3%), we again observed significantly elevated levels in the mice fed a high-fat diet which corroborated our initial findings (Figure 6d−g, Figures S27 and S28). When we compared the BL intensity and iNOS expression levels in each animal, we did not observe any correlation. This highlights the importance of activity-based sensing probes such as BL_{660}-NO since enzyme activity can be regulated by factors which are independent of protein expression (e.g., cofactor and substrate availability).

CONCLUSION

The detection of fleeting biological species, such as NO, using ABS probes *in vivo* is an immense challenge. For instance, in the context of cancer, NO levels have been reported to be less than 200 nM. We hypothesized that we could detect subtle differences in endogenous NO levels by leveraging the low intrinsic background of BL imaging, as well as reduced scattering and attenuation of emitted light in the NIR range. Although it is noteworthy that one example exists where the emission tail of the probe (λ_{em} = 599 nm) could be employed to detect fatty acid amide hydrolase activity via NIR BL imaging,[46,52] BL_{660}-NO is the first ABS probe where the λ_{em} is NIR. Upon evaluation, we found BL_{660}-NO to be selective, biocompatible, and highly sensitive as we could visualize basal levels of NO in systems ranging from cell cultures to numerous animal models.

Unlike fluorescence, photoacoustic, or chemiluminescence imaging, the generation of a BL readout requires the presence of luciferase.[35,73] In a typical BL imaging experiment, a higher signal indicates that there are more cells, and this is commonly used to track tumor progression. However, in the case of analyte sensing, the dependence on luciferase activity can confound results. Therefore, it could be difficult to discern whether a higher BL signal is due to more NO or more luciferase. To resolve this, we established a protocol where we would record the signal of BL_{660}-NO and luciferin to calculate a ratio. Because NO sensing is rate-limiting, the ratio remains the same at a given NO concentration regardless of the number of cells. These results have important implications for the development of other BL probes.

Lastly, using BL_{660}-NO in an orthotopic model of breast cancer, we were able to study the impact of a high-fat diet on the TME. Although it has long been thought that a high-fat diet can promote tumor progression by creating an abnormal inflammatory TME,[74,75] the link to NO generation has been elusive owing to a dearth of real-time detection strategies of NO *in vivo*. Our data indicates that a high-fat diet can lead to greater macrophage infiltration of the TME, which in turn generate more NO. Understanding this relationship at the molecular level can help us better combat cancer by devising strategies to reduce an inflammatory response in the TME (e.g., by developing diets with low fat for cancer prevention). Moreover, with BL_{660}-NO in hand, it is now possible to evaluate the efficacy of anti-inflammatory drugs or NO scavengers using any luciferase expressing cell line or animal model.

EXPERIMENTAL DETAILS

Synthetic Methods. *Ethyl (2E,4E)-5-(4-(Diethylamino)-phenyl)penta-2,4-dienoate (**1**).* Triethyl 4-phosphonocrotonate (1.8 mL, 7.99 mmol, 1.5 equiv) was added to a suspension of NaH (0.43 g, 10.65 mmol, 2 equiv) in anhydrous THF (10 mL) at 0 °C. The reaction was stirred at this temperature for 20 min to give an orange mixture. A solution of 4-(diethylamino)benzaldehyde (0.94 g, 5.32 mmol, 1 equiv) in anhydrous THF (4.7 mL) was added dropwise over 5 min, and it was brought to room temperature and stirred for an additional 3 h. The reaction was quenched with water and extracted with EtOAc (3×). The combined organic layers were washed with brine, dried over Na_2SO_4, filtered, concentrated, and purified via silica gel column chromatography (eluent: 4% EtOAc in hexanes) to afford **1** as a light yellow solid (0.77 g, 2.82 mmol, 53% yield). ^{1}H NMR (500 MHz, $CDCl_3$): δ 7.44 (dd, J = 15.1, 11.1 Hz, 1H), 7.33 (d, J = 8.9 Hz, 2H), 6.81 (d, J = 15.4 Hz, 1H), 6.71−6.58 (m, 3H), 5.86 (d, J = 15.2 Hz, 1H), 4.21 (q, J = 7.1 Hz, 2H), 3.38 (q, J = 7.1 Hz, 4H), 1.31 (d, J = 14.3 Hz, 3H), 1.18 (t, J = 7.1 Hz, 6H). ^{13}C NMR (125 MHz, $CDCl_3$): δ 167.74, 148.52, 146.08, 141.42, 129.07, 123.32, 121.28, 117.88, 111.51, 60.14, 44.55.

*(2E,4E)-5-(4-(Diethylamino)phenyl)penta-2,4-dienoic acid (**2**).* A 1 M solution of NaOH (2.75 mL) was added to a suspension of **1** (0.38 g, 1.39 mmol, 1 equiv) in isopropyl alcohol (11 mL) and refluxed for 8 h. The reaction was then cooled to room temperature, and the isopropyl alcohol was removed under a vacuum. The mixture was acidified with a 1 M solution of HCl and extracted with chloroform (3×), washed with brine, dried over Na_2SO_4, filtered, and concentrated to give **2** (0.34 g, 1.38 mmol, 99% yield). ^{1}H NMR (500 MHz, CD_3OD): δ 7.42 (dd, J = 15.1, 10.9 Hz, 1H), 7.36 (d, J = 8.9 Hz, 2H), 6.85 (d, J = 15.4 Hz, 1H), 6.75 (dd, J = 15.4, 10.9 Hz, 1H), 6.67 (d, J = 9.0 Hz, 2H), 5.83 (d, J = 15.1 Hz, 1H), 3.42 (q, J = 7.1 Hz, 4H), 1.17 (t, J = 7.1 Hz, 6H). ^{13}C NMR (125 MHz, CD_3OD): δ 171.30, 149.94, 148.19, 143.12, 130.11, 124.68, 122.03, 118.44, 112.65, 45.37, 12.92.

*Methyl (S)-2-((1E,3E)-4-(4-(Diethylamino)phenyl)buta-1,3-dien-1-yl)-4,5-dihydrothiazole-4-carboxylate (**3**).* A solution of **2** (0.5 g, 2.04 mmol, 1 equiv) and D-cysteine-(*S*-Trityl)-OMe (0.85 g, 2.25 mmol, 1.1 equiv) in anhydrous DMF (20.4 mL) was treated with EDC (1.32 g, 6.88 mmol,

https://doi.org/10.1021/acscentsci.1c00317
ACS Cent. Sci. 2022, 8, 461−472

3.38 equiv) and DMAP (0.64 g, 5.24 mmol, 2.56 equiv). The reaction was stirred at room temperature under N_2 for 24 h, quenched with water, and extracted with EtOAc (3×). The combined organic layers were dried over Na_2SO_4, filtered, concentrated, passed through a silica plug, and used in the next reaction without further purification. In part 2, a solution of triphenylphosphine oxide (1.12 g, 4.02 mmol, 3 equiv) in anhydrous CH_2Cl_2 (14 mL) was cooled to 0 °C under N_2. Tf_2O (0.34 mL, 2.02 mmol, 1.5 equiv) was then slowly added dropwise and stirred for 30 min. The intermediate prepared in part 1 (0.81 g, 1.34 mmol, 1 equiv) was dissolved in anhydrous CH_2Cl_2 (13 mL) and added dropwise at 0 °C. The resulting reaction mixture was stirred for 10 min, quenched with saturated $NaHCO_3$, and extracted with CH_2Cl_2 (3×). The combined organic layers were washed with brine, dried over Na_2SO_4, filtered, concentrated, and purified by silica gel column chromatography (eluent: 20% EtOAc in hexanes) to give **3** (0.58 g, 1.68 mmol, 82% yield). ^{1}H NMR (500 MHz, $CDCl_3$): δ 7.33 (d, J = 8.5 Hz, 2H), 6.94 (dd, J = 15.3, 10.2 Hz, 1H), 6.78−6.65 (m, 2H), 6.62 (d, J = 8.4 Hz, 2H), 6.52 (d, J = 15.3 Hz, 1H), 5.16 (t, J = 9.0 Hz, 1H), 3.82 (s, 3H), 3.62−3.49 (m, 2H), 3.38 (q, J = 7.0 Hz, 4H), 1.18 (t, J = 7.0 Hz, 6H). ^{13}C NMR (125 MHz, $CDCl_3$): δ 171.62, 170.42, 148.42, 144.13, 139.82, 128.96, 123.54, 122.29, 122.12, 111.57, 52.93, 44.58, 34.68, 12.77. HRMS: $[M + H]^+$ calcd for $C_{19}H_{25}N_2O_2S$, 345.1637; found, 345.1632.

*BL_{660} (**4**).* Pig liver esterase (76 mg) was added to a suspension of **3** (0.2 g, 0.58 mmol, 1 equiv) in ethanol (17 mL) and 10 mM NH_4HCO_3 (50 mL) at pH 7.8. The reaction was stirred at 37 °C for 19 h under argon. The reaction mixture was concentrated, and the residue was suspended in 1:1 v/v MeOH/$CHCl_3$. The precipitates were removed via filtration and washed. The filtrate was concentrated under a vacuum to give **4** (0.082 g, 0.248 mmol, 43% yield). ^{1}H NMR (500 MHz, CD_3OD): δ 7.37 (d, J = 8.9 Hz, 2H), 7.13−7.05 (m, 1H), 6.89−6.75 (m, 2H), 6.68 (d, J = 8.9 Hz, 2H), 6.50 (d, J = 15.1 Hz, 1H), 5.02 (t, J = 8.7 Hz, 1H), 3.67−3.55 (m, 2H), 3.42 (q, J = 7.1 Hz, 4H), 1.17 (t, J = 7.1 Hz, 6H). ^{13}C NMR (125 MHz, CD_3OD): δ 150.10, 147.22, 142.99, 130.33, 124.79, 122.69, 112.71, 78.38, 45.40, 36.07, 12.93. HRMS: $[M + H]^+$ calcd for $C_{18}H_{23}N_2O_2S$, 331.1480; found, 331.1475.

*BL_{660}-NO (**5**).* A solution of **4** (0.21 g, 0.64 mmol, 1 equiv), 1,2-phenylenediame (0.14 g, 1.29 mmol, 2 equiv), HBTU (0.24 g, 0.64 mmol, 1 equiv), and HOBt (0,097 g, 0.63 mmol, 1 equiv) in anhydrous DMF (8.0 mL) was stirred under N_2 for 5 min. DIPEA (0.11 mL, 0.63 mmol, 1 equiv) was added to the reaction mixture and stirred at room temperature overnight. The reaction was diluted with water and extracted with EtOAc (3×). Combined organic layers were dried over Na_2SO_4, filtered, concentrated, and purified using silica gel column chromatography (eluent: 1% MeOH in dichloromethane) to afford BL_{660}-NO as a dark red solid (0.088 g, 0.209 mmol, 33% yield). ^{1}H NMR (500 MHz, CD_3OD): δ 7.90 (s, 1H), 7.36 (d, J = 9.0 Hz, 2H), 7.22 (dd, J = 7.9, 1.5 Hz, 1H), 7.10−7.00 (m, 2H), 6.86 (dd, J = 8.0, 1.2 Hz, 1H), 6.80 (d, J = 8.8 Hz, 1H), 6.76−6.59 (m, 4H), 6.54 (d, J = 15.3 Hz, 1H), 5.25 (t, J = 9.2 Hz, 1H), 3.71−3.60 (m, 2H), 3.42 (q, J = 7.1 Hz, 4H), 1.17 (t, J = 7.0 Hz, 6H). ^{13}C NMR (125 MHz, CD_3OD): δ 173.33, 172.27, 149.86, 145.90, 143.30, 141.76, 132.03, 130.00, 128.46, 127.10, 124.85, 124.50, 122.76, 122.42, 119.43, 118.40, 112.67, 79.97, 49.51, 45.36, 35.66, 12.93. HRMS: $[M + H]^+$ calcd for $C_{24}H_{29}N_4OS$, 421.2062; found, 421.2047.

Analyte Selectivity Assay. The response of BL_{660}-NO (5 μM) toward a panel of biologically relevant aldehydes, reactive oxygen species, and reactive nitrogen species (75 equiv) in a 96-well culture plate was monitored using the IVIS imaging system. BL_{660}-NO was incubated with each analyte at 37 °C for 30 min before the reaction was initiated by adding ATP-$MgSO_4$ and luciferase. Light was collected immediately after mixing, and the signal enhancement was determined relative to control wells not treated with analyte. The total volume of each well was 100 μL [50 mM Tris buffer (pH 8.0) with 0.5% DMSO]. Formaldehyde solutions were prepared by depolymerizing saturated aqueous solutions at 100 °C before use. Dehydroascorbic acid was prepared by dissolving the solid in water at 65 °C before cooling to room temperature for use. Superoxide anion was added as a solution of potassium superoxide in DMSO. Nitroxyl was generated *in situ* from a solution of Angeli's salt in degassed 10 mM potassium hydroxide solution. Peroxynitrite was prepared according to the previously reported literature. NO was generated *in situ* from a solution of DEA-NONOate in degassed PBS buffer. All other analytes were prepared by dilution or dissolution from commercially available sources.

Cellular Imaging in A549-Luc2 and 4T1-Luc Cells with BL_{660}-NO. 24-well culture plates were seeded with A549-Luc2 or 4T1-Luc cells (500 μL of 400 000 cells/mL per well) and incubated at 37 °C with 5% CO_2 for 24 h. After this period, cells were ∼85% confluent. Cells were then treated with a 10 μM solution of BL_{660}-NO (0.5% DMSO final concentration) and imaged immediately using the IVIS imaging system with a 660 nm filter. To perform inhibition studies, we replaced the media with serum-free RPMI 1640 with or without L-NMMA (final concentration 1 mM). The cells were incubated for 30 min before BL_{660}-NO was applied for BL imaging.

Application of BL_{660}-NO and Luciferin for BL Imaging. 4T1-Luc cells were trypsinized, pelleted, and resuspended in serum-free RPMI 1640 media. The number of cells was determined using a Countess II automated cell counter. 200 μL of cells at a density of one, two, or three million cells/mL was added to 0.6 mL Eppendorf tubes and incubated BL_{660}-NO (10 μM) or a vehicle control (to account for the DMSO content used to solubilize BL_{660}-NO) for 15 min at 37 °C. Luciferin (0.47 mM) was then added to the tubes treated with the vehicle. DEA NONOate in degassed PBS was added to all tubes at a final concentration of 62.5, 125, or 250 μM, and the tubes were incubated for an additional 30 min at 37 °C. The tubes were then centrifuged for 2 min. The supernatant was discarded, and the cell pellet was resuspended in fresh serum-free RPMI 1640 media. The resuspended cells (100 μL) were transferred to 96-well culture plates and imaged using the IVIS imaging system using a 560 nm filter set for luciferin treated cells and a 660 nm filter set for BL_{660}-NO treated cells.

Formulation of BL_{660}-NO for *in Vivo* Imaging. BL_{660}-NO (400 μM) was dissolved in a 1:4 solution of DMSO and sterile saline (v/v) and filtered through a 0.22 μm sterile filter immediately prior to use. The typical injection volume is ∼100 μL at a dose of 0.55 mg/kg in the diet studies and 0.93 mg/kg in all other *in vivo* experiments. All *in vivo* experiments involving systemic administration utilized retro-orbital injections which is the standard technique employed by our group unless noted otherwise.

Generation of A549-Luc2 Heterotopic Lung Cancer Model. A549-Luc2 cancer cells were surgically implanted into

https://doi.org/10.1021/acscentsci.1c00317
ACS Cent. Sci. 2022, 8, 461−472

the liver of 4−5 weeks old Nu/J mice. The mice were anesthetized and aseptic technique was followed throughout the procedure. A laparotomy was performed to expose the liver. A cotton-tipped applicator was used to stabilize the lobe of the liver. The needle was inserted into the liver and slowly injected 5×10^6 cells (50 μL, 1:1 PBS/Matrigel). After injection, 5−0 Vicryl sutures were used to close the abdominal wall with 2 single interrupted sutures. Wound clips were used to close the skin and were then removed after 10 days. Tumor growth was monitored for up to 11 weeks via BL imaging.

BL Imaging of a Heterotopic Lung Cancer Model with BL_{660}-NO. Nude mice with and without A549-Luc2 tumors were treated with BL_{660}-NO (0.93 mg/kg, 20% DMSO/saline) via retro-orbital injection. After 1 h, the mice were imaged on the IVIS imaging system. Light was collected using the open filter set. An ROI was drawn around the liver, and the signal intensity was quantified using Living Image Analysis software. The counts were averaged and normalized to the non-tumor-bearing mice.

Generation of a 4T1-Luc Breast Cancer Model. Female BALB/c mice (6−8 weeks old) were inoculated with 4T1-Luc cells (100 μL of 1×10^6 cells/mL in 1:1 serum-free RPMI 1640 media and Matrigel) via subcutaneous injection into the flank. Tumor volumes were measured using the caliper method, and the body weight of the mice was monitored over the course of the experiment. After 30 days, the tumors had grown to a final volume of 300−400 mm^3.

BL Imaging of a Breast Cancer Model with BL_{660}-NO. 4T1-Luc tumor-bearing mice were treated with a sterile saline (50 μL) or a 35 mM solution of L-NMMA in sterile saline (50 μL) via intratumoral injection. After 1 h, BL_{660}-NO was administered via retro-orbital injection. After an additional hour, the mice were imaged on the IVIS imaging system. Light was collected using the 660 nm filter set. An ROI was drawn around each tumor and the signal intensity was quantified using Living Image Analysis software. Results are reported as a ratio of tumor-bearing flank over nontumor control flank.

Generation of Orthotopic 4T1-Luc Tumors and Diet Study. Female BALB/c mice (6−8 weeks old) were placed on a control diet (Research Diets no. D12450B,) or a high-fat diet (Research Diets no. D12452) where 10% or 60% of calories are from fat, respectively. After 12 (diet study 1) or 24 (diet study 2) weeks, mice were inoculated with 4T1-Luc cells (100 μL of 1×10^6 cells/mL in 1:1 serum-free RPMI 1640 media and Matrigel) via subcutaneous injection into the mammary fat pad. Each group continued receiving their respective diets until the completion of the study. Their body weights were monitored after inoculation. After ∼30 days, mice from both groups were treated with BL_{660}-NO, administered via retro-orbital injection and were imaged using the IVIS imaging system.

■ ASSOCIATED CONTENT

Supporting Information

The Supporting Information is available free of charge at https://pubs.acs.org/doi/10.1021/acscentsci.1c00317.

Further experimental details, including synthetic procedures, spectral data, and supplemental *in vitro* and *in vivo* procedures and data (PDF)

■ AUTHOR INFORMATION

Corresponding Author

Jefferson Chan − *Department of Chemistry, Beckman Institute for Advanced Science and Technology, and Cancer Center at Illinois, University of Illinois at Urbana−Champaign, Urbana, Illinois 61801, United States;* orcid.org/0000-0003-4139-4379; Email: jeffchan@illinois.edu

Authors

Anuj K. Yadav − *Department of Chemistry, Beckman Institute for Advanced Science and Technology, and Cancer Center at Illinois, University of Illinois at Urbana−Champaign, Urbana, Illinois 61801, United States*

Michael C. Lee − *Department of Chemistry, Beckman Institute for Advanced Science and Technology, and Cancer Center at Illinois, University of Illinois at Urbana−Champaign, Urbana, Illinois 61801, United States*

Melissa Y. Lucero − *Department of Chemistry, Beckman Institute for Advanced Science and Technology, and Cancer Center at Illinois, University of Illinois at Urbana−Champaign, Urbana, Illinois 61801, United States*

Shengzhang Su − *Department of Chemistry, Beckman Institute for Advanced Science and Technology, and Cancer Center at Illinois, University of Illinois at Urbana−Champaign, Urbana, Illinois 61801, United States*

Christopher J. Reinhardt − *Department of Chemistry, Beckman Institute for Advanced Science and Technology, and Cancer Center at Illinois, University of Illinois at Urbana−Champaign, Urbana, Illinois 61801, United States;* Present Address: C.J.R.: Department of Chemistry, The Skaggs Institute for Chemical Biology, The Scripps Research Institute, La Jolla, California 92037, United States; orcid.org/0000-0001-9992-1253

Complete contact information is available at: https://pubs.acs.org/10.1021/acscentsci.1c00317

Author Contributions

†A.K.Y. and M.C.L. contributed equally. A.K.Y. synthesized BL_{660}-NO and Ctrl-BL_{660}-NO; performed *in vitro* characterization, selectivity studies, and cellular imaging; and established a protocol for ratiometric calibration. M.C.L. generated the allograft breast cancer model and performed BL imaging with assistance from C.J.R. M.Y.L. generated the liver model and performed BL imaging with S.S. M.C.L. generated and performed BL imaging in the dietary-induced inflammation breast cancer model with M.Y.L. and S.S. M.Y.L. harvested and prepared tissue for immunohistostaining experiments with M.C.L. All authors analyzed and interpreted the data. A.K.Y. and J.C. wrote the manuscript. All authors have given approval to the final version of the manuscript.

Funding

This work was supported by the National Institutes of Health (R35GM133581).

Notes

The authors declare no competing financial interest.

■ ACKNOWLEDGMENTS

A.K.Y. thanks the Department of Chemistry at UIUC for a C.S. Marvel Travel Award. M.C.L. thanks the National Science Foundation for a Graduate Fellowship. M.Y.L. acknowledges the Alfred P. Sloan Foundation and the Seemon Pines Graduate Fellowship for financial support. C.J.R. thanks the

Chemistry-Biology Interface Training Grant (T32 GM070421) and the Seemon Pines Graduate Fellowship for support. Major funding for the 500 MHz Bruker CryoProbe was provided by the Roy J. Carver Charitable Trust (Muscatine, Iowa; Grant 15-4521) to the School of Chemical Sciences NMR Lab. The Q-Tof Ultima mass spectrometer was purchased in part with a grant from the National Science Foundation, Division of Biological Infrastructure (DBI-0100085). We also acknowledge Dr. Iwona Dobrucka and the Molecular Imaging Laboratory at the Beckman Institute for use of the IVIS imaging system. We thank Professor Benita Katzenellenbogen (Molecular and Integrative Physiology, UIUC) for providing 4T1-Luc mammary carcinoma cells. We also thank Mr. Joseph Reid McClure of the Division of Animal Resources for administering the research diets and Drs. Nicole Herndon and Jessica Xu for helping to generate the heterotopic lung cancer model. We also acknowledge Karen Frances Doty of the Veterinary Medicine Histology Laboratory for immunohistochemical staining.

■ ABBREVIATIONS

DEA NONOate, diethylammonium (Z)-1-(*N*,*N*-diethylamino)diazen-1-ium-1,2-diolate; EPR, electron paramagnetic resonance; L-NMMA, L-N^G-monomethyl arginine acetate; LCMS, liquid chromatography mass spectrometry; MRI, magnetic resonance imaging; PBS, phosphate buffer saline; ROI, region of interest; TLC, thin layer chromatography

■ REFERENCES

(1) Zhao, Y.; Vanhoutte, P. M.; Leung, S. W. S. Vascular Nitric Oxide: Beyond ENOS. *J. Pharmacol. Sci.* **2015**, *129* (2), 83.
(2) Yun, H.-Y.; Dawson, V. L.; Dawson, T. M. Nitric Oxide in Health and Disease of the Nervous System. *Mol. Psychiatry* **1997**, *2* (4), 300.
(3) Bogdan, C. Nitric Oxide and the Immune Response. *Nat. Immunol.* **2001**, *2* (10), 907.
(4) Shreshtha, S.; Sharma, P.; Kumar, P.; Sharma, R.; Singh, S. Nitric Oxide: It's Role in Immunity. *J. Clin. Diagn. Res.* **2018**, *12* (7), BE01−BE05.
(5) Fukumura, D.; Kashiwagi, S.; Jain, R. K. The Role of Nitric Oxide in Tumour Progression. *Nat. Rev. Cancer* **2006**, *6* (7), 521.
(6) Ridnour, L. A.; Thomas, D. D.; Switzer, C.; Flores-Santana, W.; Isenberg, J. S.; Ambs, S.; Roberts, D. D.; Wink, D. A. Molecular Mechanisms for Discrete Nitric Oxide Levels in Cancer. *Nitric Oxide* **2008**, *19* (2), 73.
(7) Lin, Y.; Xu, J.; Lan, H. Tumor-Associated Macrophages in Tumor Metastasis: Biological Roles and Clinical Therapeutic Applications. *J. Hematol. Oncol.* **2019**, *12* (1), 76.
(8) Landskron, G.; De la Fuente, M.; Thuwajit, P.; Thuwajit, C.; Hermoso, M. A. Chronic Inflammation and Cytokines in the Tumor Microenvironment. *J. Immunol. Res.* **2014**, *2014*, 1.
(9) Cranford, T. L.; Velázquez, K. T.; Enos, R. T.; Sougiannis, A. T.; Bader, J. E.; Carson, M. S.; Bellone, R. R.; Chatzistamou, I.; Nagarkatti, M.; Murphy, E. A. Effects of High Fat Diet-Induced Obesity on Mammary Tumorigenesis in the PyMT/MMTV Murine Model. *Cancer Biol. Ther.* **2019**, *20* (4), 487.
(10) Greenhill, C. High-Fat Diet and Dysbiosis Accelerate Tumorigenesis in Mice. *Nat. Rev. Endocrinol.* **2014**, *10* (11), 638.
(11) Rao, C. V.; Hirose, Y.; Indranie, C.; Reddy, B. S. Modulation of Experimental Colon Tumorigenesis by Types and Amounts of Dietary Fatty Acids. *Cancer Res.* **2001**, *61* (5), 1927−1933.
(12) Duan, Y.; Zeng, L.; Zheng, C.; Song, B.; Li, F.; Kong, X.; Xu, K. Inflammatory Links Between High Fat Diets and Diseases. *Front. Immunol.* **2018**, in press. DOI: 10.3389/fimmu.2018.02649.
(13) Bojková, B.; Winklewski, P. J.; Wszedybyl-Winklewska, M. Dietary Fat and Cancer—Which Is Good, Which Is Bad, and the Body of Evidence. *Int. J. Mol. Sci.* **2020**, *21* (11), 4114.
(14) Tsuchiya, K.; Takasugi, M.; Minakuchi, K.; Fukuzawa, K. Sensitive Quantitation of Nitric Oxide by EPR Spectroscopy. *Free Radic. Biol. Med.* **1996**, *21* (5), 733.
(15) Yoshimura, T.; Yokoyama, H.; Fujii, S.; Takayama, F.; Oikawa, K.; Kamada, H. In Vivo EPR Detection and Imaging of Endogenous Nitric Oxide in Lipopolysaccharide-Treated Mice. *Nat. Biotechnol.* **1996**, *14* (8), 992.
(16) Barandov, A.; Ghosh, S.; Li, N.; Bartelle, B. B.; Daher, J. I.; Pegis, M. L.; Collins, H.; Jasanoff, A. Molecular Magnetic Resonance Imaging of Nitric Oxide in Biological Systems. *ACS Sensors* **2020**, *5* (6), 1674.
(17) Sharma, R.; Seo, J.-W.; Kwon, S. *In Vivo* Imaging of Nitric Oxide by Magnetic Resonance Imaging Techniques. *J. Nanomater.* **2014**, *2014*, 1.
(18) Yusoff, N.; Rameshkumar, P.; Shahid, M. M.; Huang, S.-T.; Huang, N. M. Amperometric Detection of Nitric Oxide Using a Glassy Carbon Electrode Modified with Gold Nanoparticles Incorporated into a Nanohybrid Composed of Reduced Graphene Oxide and Nafion. *Microchim. Acta* **2017**, *184* (9), 3291.
(19) Gardner, S. H.; Reinhardt, C. J.; Chan, J. Advances in Activity-Based Sensing Probes for Isoform-Selective Imaging of Enzymatic Activity. *Angew. Chemie Int. Ed.* **2021**, *60*, 5000.
(20) Yadav, A. K.; Reinhardt, C. J.; Arango, A. S.; Huff, H. C.; Dong, L.; Malkowski, M. G.; Das, A.; Tajkhorshid, E.; Chan, J. An Activity-Based Sensing Approach for the Detection of Cyclooxygenase-2 in Live Cells. *Angew. Chemie Int. Ed.* **2020**, *59* (8), 3307.
(21) Gabe, Y.; Urano, Y.; Kikuchi, K.; Kojima, H.; Nagano, T. Highly Sensitive Fluorescence Probes for Nitric Oxide Based on Boron Dipyrromethene ChromophoreRational Design of Potentially Useful Bioimaging Fluorescence Probe. *J. Am. Chem. Soc.* **2004**, *126* (10), 3357.
(22) Sasaki, E.; Kojima, H.; Nishimatsu, H.; Urano, Y.; Kikuchi, K.; Hirata, Y.; Nagano, T. Highly Sensitive Near-Infrared Fluorescent Probes for Nitric Oxide and Their Application to Isolated Organs. *J. Am. Chem. Soc.* **2005**, *127* (11), 3684.
(23) Lim, M. H.; Xu, D.; Lippard, S. J. Visualization of Nitric Oxide in Living Cells by a Copper-Based Fluorescent Probe. *Nat. Chem. Biol.* **2006**, *2* (7), 375.
(24) Pluth, M. D.; McQuade, L. E.; Lippard, S. J. Cell-Trappable Fluorescent Probes for Nitric Oxide Visualization in Living Cells. *Org. Lett.* **2010**, *12* (10), 2318.
(25) Chen, Y. Recent Developments of Fluorescent Probes for Detection and Bioimaging of Nitric Oxide. *Nitric Oxide* **2020**, *98*, 1.
(26) Mao, Z.; Jiang, H.; Li, Z.; Zhong, C.; Zhang, W.; Liu, Z. An N-Nitrosation Reactivity-Based Two-Photon Fluorescent Probe for the Specific in Situ Detection of Nitric Oxide. *Chem. Sci.* **2017**, *8* (6), 4533.
(27) Reinhardt, C. J.; Zhou, E. Y.; Jorgensen, M. D.; Partipilo, G.; Chan, J. A Ratiometric Acoustogenic Probe for in Vivo Imaging of Endogenous Nitric Oxide. *J. Am. Chem. Soc.* **2018**, *140* (3), 1011−1018.
(28) Wang, S.; Li, Z.; Liu, Y.; Feng, G.; Zheng, J.; Yuan, Z.; Zhang, X. Activatable Photoacoustic and Fluorescent Probe of Nitric Oxide for Cellular and in Vivo Imaging. *Sensors Actuators B Chem.* **2018**, *267*, 403.
(29) Qi, J.; Feng, L.; Zhang, X.; Zhang, H.; Huang, L.; Zhou, Y.; Zhao, Z.; Duan, X.; Xu, F.; Kwok, R. T. K.; Lam, J. W. Y.; Ding, D.; Xue, X.; Tang, B. Z. Facilitation of Molecular Motion to Develop Turn-on Photoacoustic Bioprobe for Detecting Nitric Oxide in Encephalitis. *Nat. Commun.* **2021**, *12* (1), 960.
(30) Zhou, E. Y.; Knox, H. J.; Reinhardt, C. J.; Partipilo, G.; Nilges, M. J.; Chan, J. Near-Infrared Photoactivatable Nitric Oxide Donors with Integrated Photoacoustic Monitoring. *J. Am. Chem. Soc.* **2018**, *140* (37), 11686.
(31) Zhou, E. Y.; Knox, H. J.; Liu, C.; Zhao, W.; Chan, J. A Conformationally Restricted Aza-BODIPY Platform for Stimulus-

Responsive Probes with Enhanced Photoacoustic Properties. *J. Am. Chem. Soc.* **2019**, *141* (44), 17601.
(32) Reinhardt, C. J.; Xu, R.; Chan, J. Nitric Oxide Imaging in Cancer Enabled by Steric Relaxation of a Photoacoustic Probe Platform. *Chem. Sci.* **2020**, *11* (6), 1587.
(33) Lucero, M. Y.; East, A. K.; Reinhardt, C. J.; Sedgwick, A. C.; Su, S.; Lee, M. C.; Chan, J. Development of NIR-II Photoacoustic Probes Tailored for Deep-Tissue Sensing of Nitric Oxide. *J. Am. Chem. Soc.* **2021**, *143* (18), 7196−7202.
(34) Yadav, A. K.; Hernandez, S.; Su, S.; Chan, J. Acoustic-Based Chemical Tools for Profiling the Tumor Microenvironment. *Curr. Opin. Chem. Biol.* **2020**, *57*, 114.
(35) East, A. K.; Lucero, M. Y.; Chan, J. New Directions of Activity-Based Sensing for *in Vivo* NIR Imaging. *Chem. Sci.* **2021**, *12*, 3393.
(36) Yao, Z.; Zhang, B. S.; Prescher, J. A. Advances in Bioluminescence Imaging: New Probes from Old Recipes. *Curr. Opin. Chem. Biol.* **2018**, *45*, 148.
(37) Su, T. A.; Bruemmer, K. J.; Chang, C. J. Caged Luciferins for Bioluminescent Activity-Based Sensing. *Curr. Opin. Biotechnol.* **2019**, *60*, 198.
(38) Zhou, W.; Shultz, J. W.; Murphy, N.; Hawkins, E. M.; Bernad, L.; Good, T.; Moothart, L.; Frackman, S.; Klaubert, D. H.; Bulleit, R. F.; Wood, K. V. Electrophilic Aromatic Substituted Luciferins as Bioluminescent Probes for Glutathione S-Transferase Assays. *Chem. Commun.* **2006**, No. 44, 4620.
(39) Duellman, S. J.; Valley, M. P.; Kotraiah, V.; Vidugiriene, J.; Zhou, W.; Bernad, L.; Osterman, J.; Kimball, J. J.; Meisenheimer, P.; Cali, J. J. A Bioluminescence Assay for Aldehyde Dehydrogenase Activity. *Anal. Biochem.* **2013**, *434* (2), 226.
(40) Shah, K.; Tung, C.-H.; Breakefield, X. O.; Weissleder, R. In Vivo Imaging of S-TRAIL-Mediated Tumor Regression and Apoptosis. *Mol. Ther.* **2005**, *11* (6), 926.
(41) Vorobyeva, A. G.; Stanton, M.; Godinat, A.; Lund, K. B.; Karateev, G. G.; Francis, K. P.; Allen, E.; Gelovani, J. G.; McCormack, E.; Tangney, M.; Dubikovskaya, E. A. Development of a Bioluminescent Nitroreductase Probe for Preclinical Imaging. *PLoS One* **2015**, *10* (6), e0131037.
(42) Yao, H.; So, M.; Rao, J. A Bioluminogenic Substrate for In Vivo Imaging of β-Lactamase Activity. *Angew. Chemie Int. Ed.* **2007**, *46* (37), 7031.
(43) Juttukonda, L. J.; Green, E. R.; Lonergan, Z. R.; Heffern, M. C.; Chang, C. J.; Skaar, E. P. *Acinetobacter Baumannii* OxyR Regulates the Transcriptional Response to Hydrogen Peroxide. *Infect. Immun.* **2019**, *87* (1), e00413.
(44) Heffern, M. C.; Park, H. M.; Au-Yeung, H. Y.; Van de Bittner, G. C.; Ackerman, C. M.; Stahl, A.; Chang, C. J. In Vivo Bioluminescence Imaging Reveals Copper Deficiency in a Murine Model of Nonalcoholic Fatty Liver Disease. *Proc. Natl. Acad. Sci. U. S. A.* **2016**, *113* (50), 14219.
(45) Aron, A. T.; Heffern, M. C.; Lonergan, Z. R.; Vander Wal, M. N.; Blank, B. R.; Spangler, B.; Zhang, Y.; Park, H. M.; Stahl, A.; Renslo, A. R.; Skaar, E. P.; Chang, C. J. In Vivo Bioluminescence Imaging of Labile Iron Accumulation in a Murine Model of *Acinetobacter Baumannii* Infection. *Proc. Natl. Acad. Sci. U. S. A.* **2017**, *114* (48), 12669.
(46) Mofford, D. M.; Adams, S. T.; Reddy, G. S. K. K.; Reddy, G. R.; Miller, S. C. Luciferin Amides Enable *in Vivo* Bioluminescence Detection of Endogenous Fatty Acid Amide Hydrolase Activity. *J. Am. Chem. Soc.* **2015**, *137* (27), 8684.
(47) Cohen, A. S.; Dubikovskaya, E. A.; Rush, J. S.; Bertozzi, C. R. Real-Time Bioluminescence Imaging of Glycans on Live Cells. *J. Am. Chem. Soc.* **2010**, *132* (25), 8563.
(48) Van de Bittner, G. C.; Bertozzi, C. R.; Chang, C. J. Strategy for Dual-Analyte Luciferin Imaging: *In Vivo* Bioluminescence Detection of Hydrogen Peroxide and Caspase Activity in a Murine Model of Acute Inflammation. *J. Am. Chem. Soc.* **2013**, *135* (5), 1783.
(49) Takakura, H.; Kojima, R.; Kamiya, M.; Kobayashi, E.; Komatsu, T.; Ueno, T.; Terai, T.; Hanaoka, K.; Nagano, T.; Urano, Y. New Class of Bioluminogenic Probe Based on Bioluminescent Enzyme-Induced Electron Transfer: BioLeT. *J. Am. Chem. Soc.* **2015**, *137* (12), 4010.
(50) Iwano, S.; Obata, R.; Miura, C.; Kiyama, M.; Hama, K.; Nakamura, M.; Amano, Y.; Kojima, S.; Hirano, T.; Maki, S.; Niwa, H. Development of Simple Firefly Luciferin Analogs Emitting Blue, Green, Red, and near-Infrared Biological Window Light. *Tetrahedron* **2013**, *69* (19), 3847.
(51) Kuchimaru, T.; Iwano, S.; Kiyama, M.; Mitsumata, S.; Kadonosono, T.; Niwa, H.; Maki, S.; Kizaka-Kondoh, S. A Luciferin Analogue Generating Near-Infrared Bioluminescence Achieves Highly Sensitive Deep-Tissue Imaging. *Nat. Commun.* **2016**, *7* (1), 11856.
(52) Reddy, G. R.; Thompson, W. C.; Miller, S. C. Robust Light Emission from Cyclic Alkylaminoluciferin Substrates for Firefly Luciferase. *J. Am. Chem. Soc.* **2010**, *132* (39), 13586.
(53) Jathoul, A. P.; Grounds, H.; Anderson, J. C.; Pule, M. A. A Dual-Color Far-Red to Near-Infrared Firefly Luciferin Analogue Designed for Multiparametric Bioluminescence Imaging. *Angew. Chemie Int. Ed.* **2014**, *53* (48), 13059.
(54) Iwano, S.; Sugiyama, M.; Hama, H.; Watakabe, A.; Hasegawa, N.; Kuchimaru, T.; Tanaka, K. Z.; Takahashi, M.; Ishida, Y.; Hata, J.; Shimozono, S.; Namiki, K.; Fukano, T.; Kiyama, M.; Okano, H.; Kizaka-Kondoh, S.; McHugh, T. J.; Yamamori, T.; Hioki, H.; Maki, S.; Miyawaki, A. Single-Cell Bioluminescence Imaging of Deep Tissue in Freely Moving Animals. *Science (80-.).* **2018**, *359* (6378), 935.
(55) Hall, M. P.; Woodroofe, C. C.; Wood, M. G.; Que, I.; van't Root, M.; Ridwan, Y.; Shi, C.; Kirkland, T. A.; Encell, L. P.; Wood, K. V.; Löwik, C.; Mezzanotte, L. Click Beetle Luciferase Mutant and near Infrared Naphthyl-Luciferins for Improved Bioluminescence Imaging. *Nat. Commun.* **2018**, *9* (1), 132.
(56) Zambito, G.; Hall, M. P.; Wood, M. G.; Gaspar, N.; Ridwan, Y.; Stellari, F. F.; Shi, C.; Kirkland, T. A.; Encell, L. P.; Löwik, C.; Mezzanotte, L. Red-Shifted Click Beetle Luciferase Mutant Expands the Multicolor Bioluminescent Palette for Deep Tissue Imaging. *iScience* **2021**, *24* (1), 101986.
(57) Knox, H. J.; Kim, T. W.; Zhu, Z.; Chan, J. Photophysical Tuning of *N* -Oxide-Based Probes Enables Ratiometric Photoacoustic Imaging of Tumor Hypoxia. *ACS Chem. Biol.* **2018**, *13* (7), 1838.
(58) Zheng, H.; Shang, G.-Q.; Yang, S.-Y.; Gao, X.; Xu, J.-G. Fluorogenic and Chromogenic Rhodamine Spirolactam Based Probe for Nitric Oxide by Spiro Ring Opening Reaction. *Org. Lett.* **2008**, *10* (12), 2357.
(59) Ikeda, Y.; Nomoto, T.; Hiruta, Y.; Nishiyama, N.; Citterio, D. Ring-Fused Firefly Luciferins: Expanded Palette of Near-Infrared Emitting Bioluminescent Substrates. *Anal. Chem.* **2020**, *92* (6), 4235.
(60) Xu, Y.; Shi, D.; Wang, X.; Yu, S.; Yu, X.; Pu, L. Development of Aldehyde-Based Fluorescent Probes for Highly Selective Recognition of 1,3-Diaminopropane. *Eur. J. Org. Chem.* **2017**, *2017* (33), 4990.
(61) Dilek, O.; Bane, S. Turn on Fluorescent Probes for Selective Targeting of Aldehydes. *Chemosensors* **2016**, *4* (1), 5.
(62) Fu, Y.; Gao, Y.; Chen, L.; He, Q.; Zhu, D.; Cao, H.; Cheng, J. Highly Efficient Single Fluorescent Probe for Multiple Amine Vapours via Reaction between Amine and Aldehyde/Dioxaborolane. *RSC Adv.* **2014**, *4* (87), 46631.
(63) Wong, V.; Lerner, E. Nitric Oxide Inhibition Strategies. *Futur. Sci. OA* **2015**, in press. DOI: 10.4155/fso.15.35.
(64) Le Guennec, D.; Hatte, V.; Farges, M.-C.; Rougé, S.; Goepp, M.; Caldefie-Chezet, F.; Vasson, M.-P.; Rossary, A. Modulation of Inter-Organ Signalling in Obese Mice by Spontaneous Physical Activity during Mammary Cancer Development. *Sci. Rep.* **2020**, *10* (1), 8794.
(65) Hermano, E.; Goldberg, R.; Rubinstein, A. M.; Sonnenblick, A.; Maly, B.; Nahmias, D.; Li, J.-P.; Bakker, M. A. H.; van der Vlag, J.; Vlodavsky, I.; Peretz, T.; Elkin, M. Heparanase Accelerates Obesity-Associated Breast Cancer Progression. *Cancer Res.* **2019**, *79* (20), 5342.
(66) Soldati, L.; Di Renzo, L.; Jirillo, E.; Ascierto, P. A.; Marincola, F. M.; De Lorenzo, A. The Influence of Diet on Anti-Cancer Immune Responsiveness. *J. Transl. Med.* **2018**, *16* (1), 75.

(67) Kado, T.; Nawaz, A.; Takikawa, A.; Usui, I.; Tobe, K. Linkage of CD8+ T Cell Exhaustion with High-Fat Diet-Induced Tumourigenesis. *Sci. Rep.* **2019**, *9* (1), 12284.
(68) Wang, K.; Sun, J.-Z.; Wu, Q.-X.; Li, Z.-Y.; Li, D.-X.; Xiong, Y.-F.; Zhong, G.-C.; Shi, Y.; Li, Q.; Zheng, J.; Shivappa, N.; Hébert, J. R.; Foukakis, T.; Zhang, X.; Li, H.-Y.; Xiang, T.-X.; Ren, G.-S. Long-Term Anti-Inflammatory Diet in Relation to Improved Breast Cancer Prognosis: A Prospective Cohort Study. *npj Breast Cancer* **2020**, *6* (1), 36.
(69) Hayashi, T.; Fujita, K.; Nojima, S.; Hayashi, Y.; Nakano, K.; Ishizuya, Y.; Wang, C.; Yamamoto, Y.; Kinouchi, T.; Matsuzaki, K.; Jingushi, K.; Kato, T.; Kawashima, A.; Nagahara, A.; Ujike, T.; Uemura, M.; Pena, M. D. C. R.; Gordetsky, J. B.; Morii, E.; Tsujikawa, K.; Netto, G. J.; Nonomura, N. High-Fat Diet-Induced Inflammation Accelerates Prostate Cancer Growth via IL6 Signaling. *Clin. Cancer Res.* **2018**, *24* (17), 4309.
(70) Sieri, S.; Chiodini, P.; Agnoli, C.; Pala, V.; Berrino, F.; Trichopoulou, A.; Benetou, V.; Vasilopoulou, E.; Sánchez, M.-J.; Chirlaque, M.-D.; Amiano, P.; Quirós, J. R.; Ardanaz, E.; Buckland, G.; Masala, G.; Panico, S.; Grioni, S.; Sacerdote, C.; Tumino, R.; Boutron-Ruault, M.-C.; Clavel-Chapelon, F.; Fagherazzi, G.; Peeters, P. H. M.; van Gils, C. H.; Bueno-de-Mesquita, H. B.; van Kranen, H. J.; Key, T. J.; Travis, R. C.; Khaw, K. T.; Wareham, N. J.; Kaaks, R.; Lukanova, A.; Boeing, H.; Schütze, M.; Sonestedt, E.; Wirfält, E.; Sund, M.; Andersson, A.; Chajes, V.; Rinaldi, S.; Romieu, I.; Weiderpass, E.; Skeie, G.; Dagrun, E.; Tjønneland, A.; Halkjær, J.; Overvard, K.; Merritt, M. A.; Cox, D.; Riboli, E.; Krogh, V. Dietary Fat Intake and Development of Specific Breast Cancer Subtypes. *JNCI J. Natl. Cancer Inst.* **2014**, *106* (5), dju068.
(71) Bruder-Nascimento, T.; Ekeledo, O. J.; Anderson, R.; Le, H. B.; Belin de Chantemèle, E. J. Long Term High Fat Diet Treatment: An Appropriate Approach to Study the Sex-Specificity of the Autonomic and Cardiovascular Responses to Obesity in Mice. *Front. Physiol.* **2017**, in press. DOI: 10.3389/fphys.2017.00032.
(72) van der Heijden, R. A.; Sheedfar, F.; Morrison, M. C.; Hommelberg, P. P.; Kor, D.; Kloosterhuis, N. J.; Gruben, N.; Youssef, S. A.; de Bruin, A.; Hofker, M. H.; Kleemann, R.; Koonen, D. P.; Heeringa, P. High-Fat Diet Induced Obesity Primes Inflammation in Adipose Tissue Prior to Liver in C57BL/6j Mice. *Aging (Albany. NY).* **2015**, *7* (4), 256−268.
(73) Sadikot, R. T. Bioluminescence Imaging. *Proc. Am. Thorac. Soc.* **2005**, *2* (6), 537.
(74) Larionova, I.; Tuguzbaeva, G.; Ponomaryova, A.; Stakheyeva, M.; Cherdyntseva, N.; Pavlov, V.; Choinzonov, E.; Kzhyshkowska, J. Tumor-Associated Macrophages in Human Breast, Colorectal, Lung, Ovarian and Prostate Cancers. *Front. Oncol.* **2020**, in press. DOI: 10.3389/fonc.2020.566511.
(75) Cassetta, L.; Fragkogianni, S.; Sims, A. H.; Swierczak, A.; Forrester, L. M.; Zhang, H.; Soong, D. Y. H.; Cotechini, T.; Anur, P.; Lin, E. Y.; Fidanza, A.; Lopez-Yrigoyen, M.; Millar, M. R.; Urman, A.; Ai, Z.; Spellman, P. T.; Hwang, E. S.; Dixon, J. M.; Wiechmann, L.; Coussens, L. M.; Smith, H. O.; Pollard, J. W. Human Tumor-Associated Macrophage and Monocyte Transcriptional Landscapes Reveal Cancer-Specific Reprogramming, Biomarkers, and Therapeutic Targets. *Cancer Cell* **2019**, *35* (4), 588.
(76) Lucero, M. Y.; Chan, J. Photoacoustic imaging of elevated glutathione in models of lung cancer for companion diagnostic applications. *Nature Chem.* **2021**, *13*, 1248.

https://doi.org/10.1021/acscentsci.1c00317
ACS Cent. Sci. 2022, 8, 461−472